Ng, KH., Tameh, EK., Doufexi, A., Hunukumbure, MR., & Nix, AR. (2007). Efficient multielement ray tracing with site-specific comparisons using measured MIMO channel data. *IEEE Transactions on Vehicular Technology*, *56*(3), 1019 - 1032. https://doi.org/10.1109/TVT.2007.895606

Peer reviewed version

Link to published version (if available):
10.1109/TVT.2007.895606

Efficient Multielement Ray Tracing With Site-Specific Comparisons Using Measured MIMO Channel Data

Kah Heng Ng, Eustace K. Tameh, Angela Doufexi, Mythri Hunukumbure, and Andrew R. Nix

***Abstract*—In this paper, an advanced site-specific image-based ray-tracing model is developed that enables multielement outdoor propagation analysis to be performed in dense urban environments. Sophisticated optimization techniques, such as preprocessing the environment database using object partitioning, visibility determination, diffraction image tree precalculation, and parallel processing are used to improve run-time efficiency. Wideband and multiple-input–multiple-output (MIMO) site-specific predictions (including derived parameters such as theoretic capacity and eigenstructure) are compared with outdoor site-specific measurements at 1.92 GHz. Results show strong levels of agreement, with a mean path-loss error of 2 dB and a mean normalized-capacity error of 1.5 b/s/Hz. Physical-layer packet-error rate (PER) results are generated and compared for a range of MIMO-orthogonal frequency-division-multiplexing (OFDM) schemes using measured and predicted multielement channel data. A mean E_b/N_0 error (compared to PER results from measured channel data) of 4 and 1 dB is observed for spatial-multiplexing and space-time block-code schemes, respectively. Results indicate that the ray-tracing model successfully predicts key channel parameters (including MIMO channel structure) and thus enable the accurate prediction of PER and service coverage for emerging MIMO-OFDM networks such as 802.11n and 802.16e.**

***Index Terms*—Multiple-input–multiple-output (MIMO), propagation, ray tracing, scattering.**

I. Introduction

MULTIPLE-ANTENNA systems that employ one or more elements at both the transmitter and receiver have the potential to greatly enhance the data capacity of a wireless-communication network. The exploitation of spatial and/or temporal diversity in a multiple-input–multiple-output (MIMO) communication system offers considerable benefit [1]–[4]. Such systems fuse the antenna, modulation, coding, and detection stages to directly exploit the features present in multichannel propagation links. Such systems generally make use of space-time coding and/or spatial-multiplexing (SM) algorithms in their implementations [5]–[14]. The high-frequency approximation of electromagnetic-wave propagation based on geometric optics (GOs) allows ray tracing to be used to predict the radio channel between any two points. This is the basis of all deterministic propagation models [15]–[21]. The major drawback of ray-tracing models is their computational cost, which depends on factors such as the size and complexity of the geographic database and the interaction order in the ray search. Ray models must tradeoff prediction accuracy for run-time efficiency. Nevertheless, many ray-tracing models have been developed over the years and many have shown good agreement with measured channel characteristics for single-antenna systems [16]–[21].

The conventional ray-tracing model for a single-antenna system performs a point-to-point analysis between the transmitter and receiver. For multiple-antenna systems, the ray-tracing operation can be performed for each and every transmitter and receiver link. This brute-force approach can be tedious, and the required processing time is linearly proportional to the product of the number of transmitter and receiver elements. Hence, optimization techniques that reduce computational time are vital for MIMO ray-tracing tools.

In this paper, an advanced multielement ray-tracing model is presented. Site-specific comparison is then performed between the model's output and a range of measured outdoor MIMO channels. To the best of our knowledge, no similar comparison study using measured and predicted multielement channel data is reported in the literature. Furthermore, this paper continues to analyze site-specific packet-error rate (PER) predictions for several MIMO-orthogonal frequency-division-multiplexing (OFDM) schemes using measured and predicted channel data. The ability to accurately predict the performance of MIMO-OFDM schemes in urban environments is of particular relevance to the rollout and deployment of 802.11n and 802.16e networks.

This paper is organized as follows. In Section II, the multielement ray-tracing model is described. Next, the database and the various optimization techniques are introduced. In Section III, the MIMO measurement configuration is described. In Section IV, the measured data sets are compared with our predicted MIMO output for a variety of site-specific locations. Various channel parameters and MIMO characteristics are studied, including the derived eigenstructure and theoretic capacity. A unique PER comparison study (using measured and predicted channel data) is reported based on an example SM and

Manuscript received January 17, 2005; revised August 23, 2005, December 16, 2005, and April 5, 2006. The work of K. H. Ng was supported in part by the IST-2001-32549 ROMANTIK Project. The review of this paper was coordinated by Dr. K. Dandekar.

K. H. Ng is with the Picochip Designs Ltd., BA1 5BG Bath, U.K. (e-mail: k.h.ng@bris.ac.uk).

E. K. Tameh, A. Doufexi, M. Hunukumbure, and A. R. Nix are with the University of Bristol, BS1 1UB Bristol, U.K. (e-mail: k.h.ng@bris.ac.uk; tek.tameh@bris.ac.uk; a.doufexi@bris.ac.uk; mythri.hunukumbure@bris.ac.uk; andy.nix@bris.ac.uk).

Color versions of one or more of the figures in this paper are available online at http://ieeexplore.ieee.org.

Digital Object Identifier 10.1109/TVT.2007.895606

space-time block-code (STBC) extensions to IEEE 802.11a [22]. This paper ends with a set of conclusions.

II. Multielement Ray-Tracing Model

A. Ray Model

The ray-tracing model uses a rigorous image-based approach to generate ray paths and is capable of performing an extensive ray-path search [23]–[26]. Supported propagation mechanisms include building reflection, building rooftop diffraction, building corner diffraction, building scattering, terrain scattering, and combinations of the above. Ray paths are calculated in full 3-D geometry. A new heuristic geometrical approach for finding noncoplanar multiple-edge diffraction ray paths is supported to overcome limitations in the conventional image-based technique [26]. This method has been shown [26] to reduce errors in the predicted path loss by up to 1 dB. A novel hybrid GOs and radiance-based scattering model is also implemented to model the scattering effects from rough surfaces (which can be significant in MIMO systems). In [25], this scatter model was shown to improve the mean path-loss prediction by up to 2.7 dB when compared to conventional models. A vertical-plane diffraction model is supplemented to approximate higher order building rooftop diffractions for faster processing [18]. The capability of the ray model to combine these key propagation mechanisms allows comprehensive analysis to be performed in dense urban environments. Fig. 1 shows a flowchart for the operation of the ray-tracing model. The model can be divided into four sections [23]: 1) preprocessing of the database; 2) creation of the image tree; 3) creation of the ray tree; and 4) electromagnetic calculation. Preprocessing of the database is required to perform a one-time optimization of the environment database, in order to accelerate the ray-path-finding process at run-time. The ray-path-finding process is used to identify all possible ray paths from the transmitter to the receiver. This process includes the forward creation of image trees and the creation of ray trees through backward tracing, which are typical in an image-based ray-tracing model. The electromagnetic-calculation stage applies various electromagnetic models, such as the use of GO Fresnel reflection coefficients, uniform theory of diffraction (UTD) with slope diffraction, the International Telecommunication Union-Radiocommunication Sector foliage-loss model, and a hybrid scattering model, to each ray [15], [25], [27]–[29].

B. Database

The 3-D object geometry used in the ray-tracing model consists of polygons, polygon tiles, polygon horizontal edges, polygon vertical edges, and terrain height grids. This is similar to the definitions found in [19]. The difference here is that, in [19], edges are divided into segments and all interactions (reflection and diffraction) occur at the center of every visible tile and segment. In the ray-tracing model described here, the visible center of polygon tiles are used for scattering, polygons are used for reflection, polygon horizontal and vertical edges are used for diffraction, and terrain height grids are used for scattering. This avoids the need to break down the polygons into

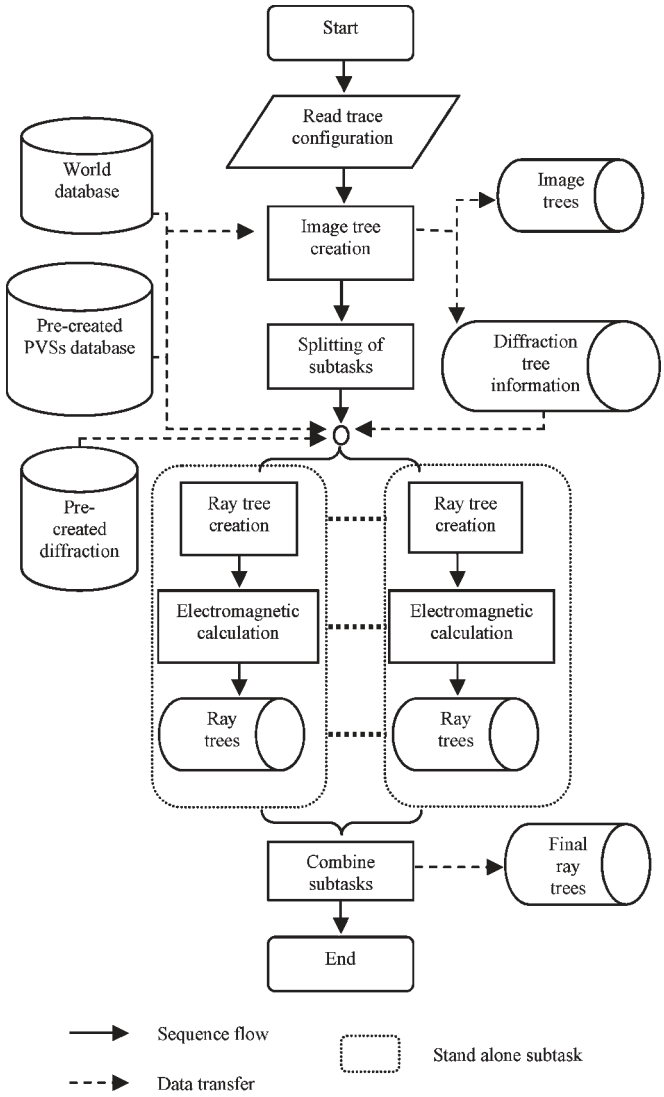

Fig. 1. Flow chart of ray-tracing model.

segments and tiles for reflection and diffraction purposes due to the nature of image-based ray tracing. This reduces the number of interaction objects. For example, when considering reflection from one potential visible polygon surface, Wolfle *et al.* [19] has to perform calculations at every visible center of a tile, whereas, in our approach, only one reflection calculation is needed, and this saves significant computation time.

C. Optimization Techniques

A number of advanced acceleration techniques are implemented, including object space partitioning, visibility determination, precreation of edge diffraction trees, and grid computing. Some of these techniques have greatly enhanced the efficiency of the ray-tracing process [30]–[32]. These techniques are performed during the database preprocessing stage to accelerate the ray-path-finding process without any loss of accuracy (a more detailed description and a discussion of the advantages of these techniques can be found in [23]).

1) Object Space Partitioning: Object space partitioning is an effective spatial-partitioning method for creating powerful data structures that enable fast object spatial handling [33].

For databases with many objects, object space partitioning can greatly accelerate spatial operations such as proximity queries, ray casting, and ray intersections. A hybrid intraobject binary-space-partition (BSP) tree and interobject quadtree data structure is implemented here. Each object (building and foliage) is partitioned into individual BSP trees. All the BSP trees in turn are partitioned into a single quadtree. The reason for using a hybrid spatial-partitioning method arises from the fact that the use of a BSP in a complicated outdoor environment creates many implementation problems (particularly, floating point errors), and a volume-bounding quadtree does not include information about the polygons in each object. Since the BSP tree is already constructed for each object for constructive solid geometry purposes (i.e., for building a 3-D world from the raw database) [33], the hybrid method is feasible to combine the powerful features of both a BSP and quadtree. This is different from the techniques used in the study in [30]–[32], where only one type of object space partitioning has been implemented. A comparison test performed in the study in [23] showed that object space partitions using the hybrid method improves processing time by 192% and 44% compared to the simple intersection and quadtree methods, respectively.

2) Visibility Determination: One way to improve the efficiency of a ray-tracing algorithm is to reject objects early when ray intersection is impossible. The result of visibility determination can be stored in a data structure known as the potential visibility set (PVS). A PVS is a set of potential visible information [34]. It is basically a table of simple "Yes" or "No" entries on object visibility. For ray-tracing purposes, it is important to have a set of PVSs for interobject and point-object visibility. Interobject PVSs allows fast visibility determination for rays between objects. Point-object PVSs determine the visibility of objects from emitter points. These PVSs are compressed using simple zero-run-length coding [34] for optimal storage and fast access during run-time. Visibility determination using effective object occlusion culling is implemented in this ray model (details of the method used can be found in [23]). Basically, the technique uses a set of clipping planes created by an observation point to an occluder to eliminate objects that fall within the shadowed region. The concept of visibility determination is slightly different to the general angular Z-buffer (AZB) technique [35]. In the AZB technique, the viewpoint can be a transmitter (Tx) or an image. When a ray is launched from the viewpoint, only those objects located in the angular region containing the ray need to be tested for ray intersection. This method accelerates the ray-tracing algorithm, but when higher order ray interactions are needed, the required preprocessing is complex [36]. This occurs because there are many source points (including the Tx and a large number of its images), and an AZB is required for each of them. On the contrary, the main purpose of the occlusion-culling technique used here is to calculate the interobject PVS during the preprocessing stage, regardless of the order of interaction. Hence, our method can accelerate the ray-intersection test and, more importantly, perform early elimination of unnecessary images.[1] A reduction in visibility results in an improvement in the speed of the ray-tracing process as less object interactions are performed. Fig. 2 shows the potential visible front-facing polygons (shaded white) from a given viewpoint S. Only objects shaded white are used for ray-interaction purposes.

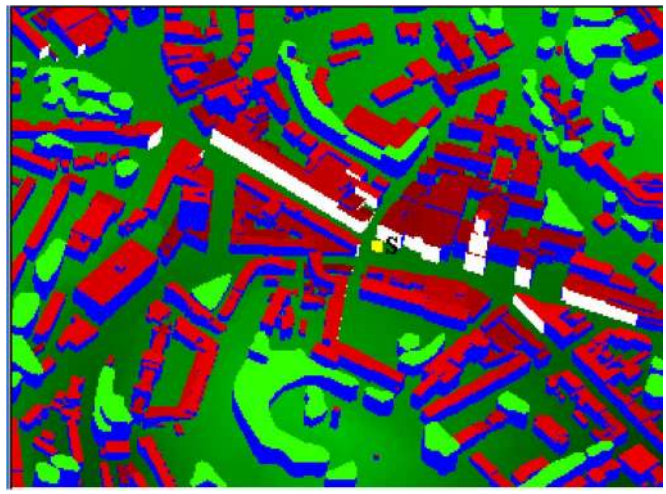

Fig. 2. Point to polygon visibility.

3) Precreation of Diffraction Trees: For image-based ray tracing, generating images and storing the image trees is computationally costly. An image tree is formed based on the knowledge of the source position and an object database. The source is either a transmitter or a vertical diffraction edge. The overall image tree for each ray-tracing run consists of one transmitter image tree with branches of diffraction image trees at each visible diffraction edge. As all diffraction-edge source positions are static for each environment database, their 2-D diffraction image trees (which contain 2-D images without height) are the same for each ray-tracing run (regardless of the transmitter position). Therefore, it is possible to precreate all the diffraction image trees for each database. These precreated diffraction image trees are dynamically linked at run-time. One constraint of this technique is that the maximum order of reflection after diffraction for each ray is limited by the order of the static diffraction image tree (as with all image trees). Nevertheless, if a high order of reflection after diffraction is required, then it is possible to expand the precreated diffraction tree at run-time at the expense of speed.

Fig. 3(a) shows an image tree with solid-shaded circles representing reflection and dashed shaded circles representing diffraction. Three of the diffraction nodes have the same diffraction edge, and hence, they have the same child tree. Fig. 3(b) shows that this redundancy is removed by dynamic linking to a precreated diffraction tree. Note that a typical single-element image tree (including diffraction trees) is around 100 MB for the studies reported here. This compares to around 25 MB when precreated diffraction image trees are used.

4) Grid Computing: One advantage of image-based ray tracing is that the same image tree can be used in the creation of all ray trees with the same trace configuration. A typical ray-tracing application has many receiver points (ray trees), and this provides a way to exploit parallel processing. The ray-tracing model, which is discussed here, can split the creation of the ray

[1]Note that the visibility tree information (i.e., the PVS) can also be calculated using the AZB technique by considering the object as viewpoints.

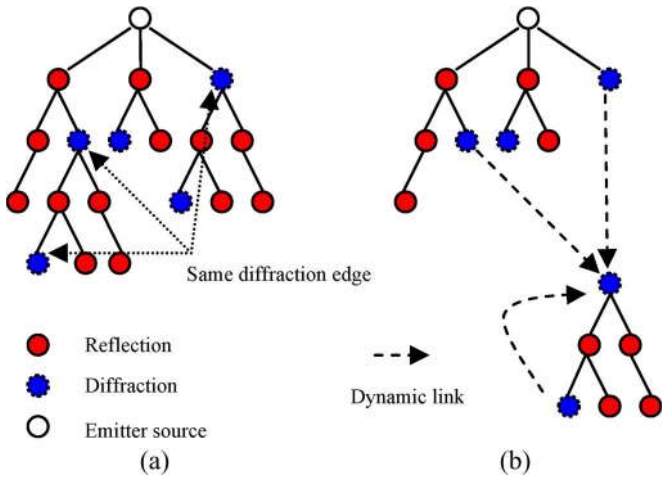

Fig. 3. Precreation of diffraction trees.

trees into multiple subtasks, each handling a number of receiver points. Each subtask is capable of performing stand-alone ray tracing with the same image tree. Hence, the whole ray-tracing process can be distributed into multiple subtasks for the grid-computing process (see Fig. 1). This greatly enhances the speed of the ray-tracing process and makes it feasible to perform rapid route and grid analysis. The only insignificant overhead is the need to combine subtask results into a single structure. The speed of ray tracing can be improved linearly with the number of grid-computing processors. In [23], a comparison test using ten processors was performed and the use of grid-computing reduced run-time by around 850%.

D. Implementation of MIMO Ray Tracing

When multiple-antenna systems are used in a deterministic ray model, the computational cost of the resulting MIMO prediction is a major drawback. In [24], two MIMO modeling approaches were investigated. Both methods made use of an enhanced deterministic ray-tracing propagation model. The first method relied on point-to-point prediction for each of the multiple element-to-element links. The second approach estimated the MIMO link matrix from a single point-to-point ray-tracing study. A comparison of normalized capacity and path loss was performed for the two methods in an outdoor city-center environment. A comparison with the measured array data was also reported, and the results showed that the single point-to-point approximation worked well and could significantly reduce run-time when compared to the full element-to-element prediction approach. The ray-tracing model used here supports both techniques.

III. Validation Trial Setup

A. Measurement Scenario

The measurements used for comparison were conducted in and around the University of Bristol precinct (see Fig. 4) [37]. The receiving antennas were located at a number of sites in Berkeley Square, which is surrounded by commercial and residential buildings, to provide a mixture of line-of-sight

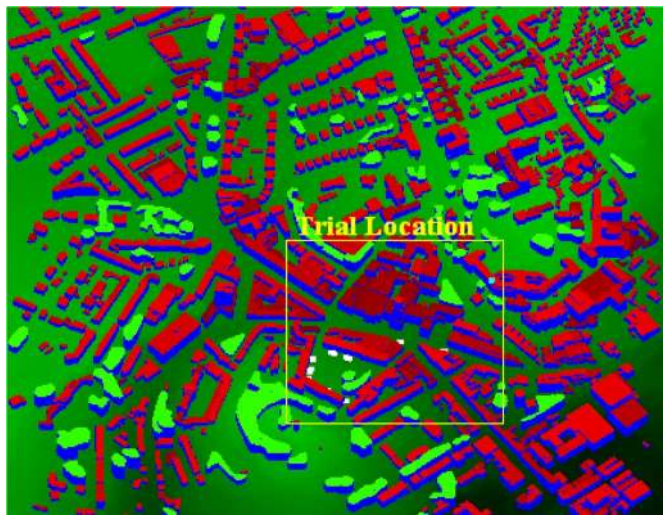

Fig. 4. Trial location in the city of Bristol.

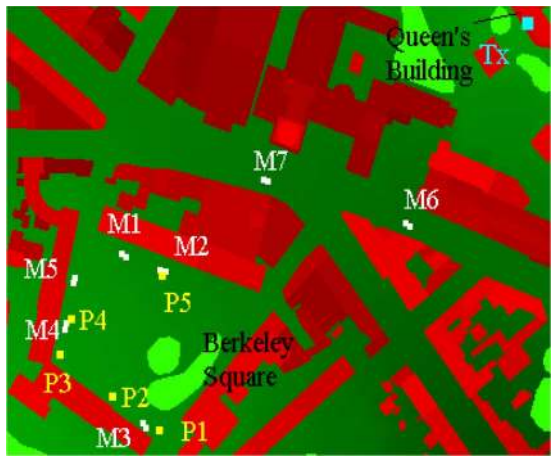

Fig. 5. Measurement locations showing static points P1–P5 and moving routes M1–M7.

(LoS) and nonline-of-sight (NLoS) measurement points. The transmitting antennas were mounted on the roof of Queen's Building, facing toward the square, well above the mean level of the local clutter (at a bore sight of about -140°). The mean distance from the transmit site to Berkeley Square is around 300 m. The five point (P) and seven moving (M) measurements were taken during the trial campaign. The moving measurements covered a distance of 2–3 m at a mobile speed of 10–15 km/h (a full summary of the measurement types and their locations is given in Fig. 5). The point measurements consist of 800 MIMO snapshots, while the moving measurements consist of 128 MIMO snapshots.

The measurements were performed using a Medav Channel Sounder [37], [45]. A bandwidth of 20 MHz at a center frequency of 1.92 GHz was used. The frequency resolution was 156.25 kHz. The transmit output power was 36 dBm. The transmitting antennas used two commercially available dual polarized $(\pm 45^\circ)$ UMTS panel antennas [see Fig. 6(a)]. These antennas offered a 17-dBi gain, with 20 dB of cross-polar discrimination. The antennas were mounted on the rooftop, spaced 3.12 m (or 20λ) apart and with 8° of mechanical down tilt.

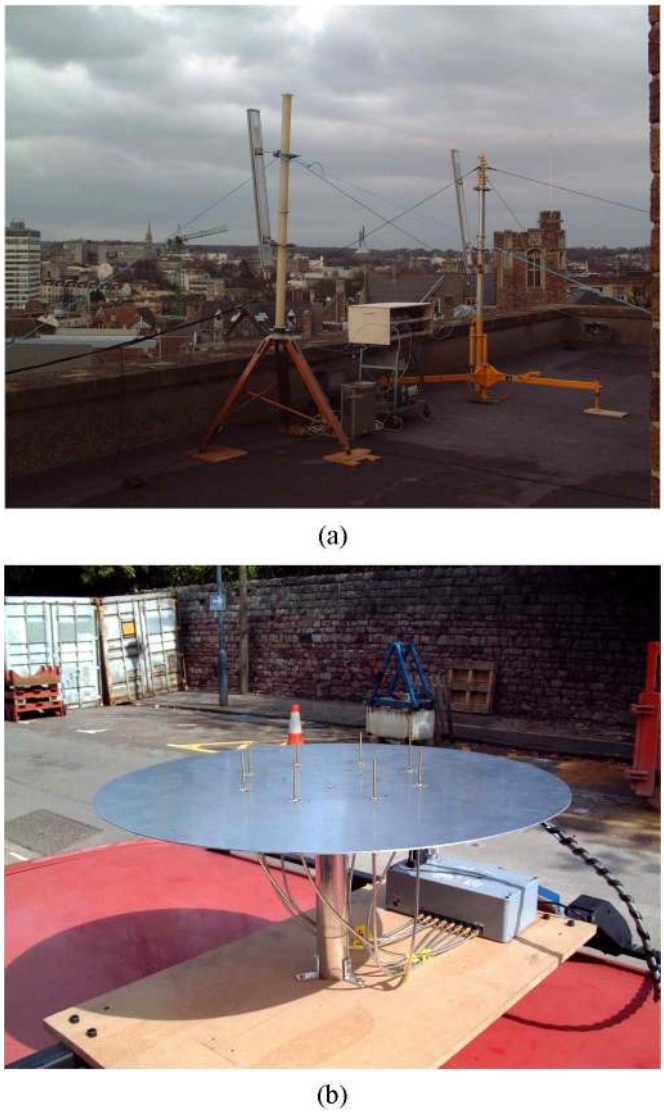

Fig. 6. (a) Transmitter mounted on building top. (b) UCA receiver mounted on car top.

The half power azimuth beamwidth was 65°, and the vertical beamwidth was 7°. The receiving antennas used a uniform circular array, made up of eight omnidirectional monopoles mounted on the top of a vehicle at approximately 1.7 m from the ground [see Fig. 6(b)]. The interelement spacing was 0.5λ. This circular array was designed and constructed at the University of Bristol. Given four transmit ports $(\pm 45^\circ \times 2)$ and eight receive ports, each measurement snapshot results in a 4×8 MIMO channel matrix.

B. Ray-Tracing Model Setup

A 1-km by 1-km area of central Bristol is represented in the model using the geographic database shown in Fig. 4. Building and foliage are represented as flat-topped vectorized polygonal objects. Terrain is sampled at 10-m resolution. The database consists of 995 buildings, 174 foliage objects, 12 495 building polygons, 61 733 building polygon tiles, 7921 building corner edges, and 14 046 terrain pixels.

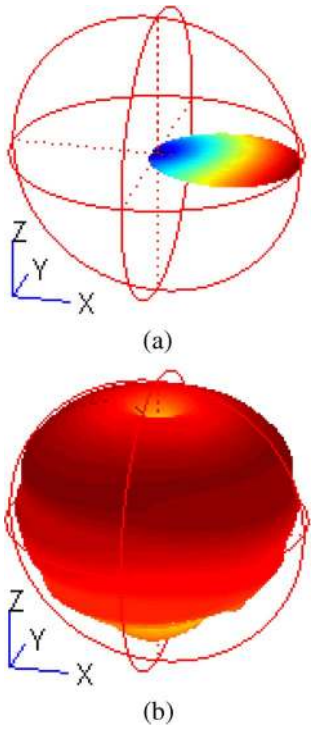

Fig. 7. (a) Synthesized pattern for transmitter. (b) Measured monopole.

The transmitting antenna-element patterns used for the prediction analysis were produced synthetically (since the size of the antenna made it very difficult to measure), as shown in Fig. 7(a). The pattern-synthesis technique in [38] was used to generate antenna patterns that closely match the antenna specifications used in practice. For the receiving monopole element, isolated monopole patterns measured in the University of Bristol's anechoic chamber were used, as shown in Fig. 7(b).

Ray-tracing operations are performed up to four orders of reflection and two orders of diffraction. Foliage loss, building scatter, and terrain scatter were all included. The electrical properties of the buildings and terrain are given in Table I, with typical parameters used from the literature [39]–[42].

Ray-tracing produces ray results with infinite resolution in all domains, i.e., delay/frequency, time/Doppler, and angular/spatial [43]–[45]. Thus, before performing any practical analysis in any of these domains, the ray results are processed to have the same resolution as the target physical-layer system. This process is referred to as band limiting or binning. The band-limiting process of a 1-D channel in the time-delay/frequency-domain model is shown as follows:

$$H_k = \sum_{i=0}^{N-1} \gamma_i e^{-2\pi j(k-1)(\Delta f)(\tau_i)} \tag{1}$$

where H_k is the kth channel-frequency-response sample, k is the channel-frequency-response sample number, N is the total number of rays, Δf is the frequency resolution, which is determined by the maximum excess delay (or the Doppler domain resolution), τ_i is the time delay of the $(i+1)$th ray, and γ_i is the complex E field of the $(i+1)$th ray. Equation (1) assumes an ideal rectangular filter in the frequency domain [46]. In order to

TABLE I
ELECTRICAL PROPERTIES OF DATABASE OBJECTS

	Relative permittivity	Conductivity (S/m)	Surface roughness [25] (m)
Building wall	7	0.001	0.02
Building top	10	0.02	0.01
Terrain	15	0.05	0.02

transform the channel into the time domain, a Fourier transform can be used. The time-delay resolution can be determined by the system bandwidth. For higher dimensional channels, such as directional channels (which include spatial/angular domains), a similar process is performed to resolve the ray results in each domain.

For predicting static points, one method of generating multiple-channel realizations is to randomize the location of the antennas in a small local area (in the dimension of wavelengths) to simulate the spatial sensitivity of the scattering environment [46]. This brute-force method can be time consuming due to the need to repeat the ray-tracing process. Hence, to generate further channel realizations, we synthetically change the phase of the predicted ray paths according to a uniform randomly distributed displacement of the antennas. Given M transmitters, N receivers, and R realizations, the transfer function from the mth transmitter to the nth receiver in the rth realization for the fth channel frequency-response sample is

$$H_{m,n}(f,r) = \sum_{i=0}^{K-1} a_i \exp\left[j\left(\alpha_i - 2\pi(f-1)\Delta f \tau_i + \beta(r,i)\right)\right] \tag{2}$$

$$\beta(r,i) = \frac{2\pi}{\lambda}\left(\overline{D}(i)\cdot\overline{\mathrm{LT}}(r) + \overline{A}(i)\cdot\overline{\mathrm{LR}}(r)\right) \tag{3}$$

$$\overline{D}(i) = \sin\left(\vartheta_d(i)\right)\cos\left(\varphi_d(i)\right)\hat{x} + \sin\left(\vartheta_d(i)\right)\sin\left(\varphi_d(i)\right)\hat{y} + \cos\left(\vartheta_d(i)\right)\hat{z} \tag{4}$$

$$\overline{A}(i) = \sin\left(\vartheta_a(i)\right)\cos\left(\varphi_a(i)\right)\hat{x} + \sin\left(\vartheta_a(i)\right)\sin\left(\varphi_a(i)\right)\hat{y} + \cos\left(\vartheta_a(i)\right)\hat{z} \tag{5}$$

where a_i, α_i, and τ_i represent the magnitude, phase, and time delay of the ith ray, K is the total number of rays, Δf is the frequency resolution, β is the phase displacement, $\overline{\mathrm{LT}}$ and $\overline{\mathrm{LR}}$ are the random uniformly distributed displacement vectors for the transmitter and receiver, respectively, and $\overline{D}$ and $\overline{A}$ are the departure and arrival directional vectors of the ith ray. ϑ and φ refer to the angles shown in Fig. 8. The subscripts d and a denote the departure and arrival angles, respectively. Note that the random displacement vectors $\overline{\mathrm{LT}}$ and $\overline{\mathrm{LR}}$ must remain unchanged for different antennas m and n.

The synthesis technique, which is described in (2), is derived from the principle of phase changes due to small-scale spatial displacement [46]. It is different from the technique given in [47]. In [47], multipath components (MPCs) are derived from the measurements, and a set of random uniformly distributed phases are applied to all MPCs, thereby generating different realizations. Each antenna element has the same number of MPCs, and the same random phase is applied to each antenna element. Although this approximate technique of applying random phase is fast, in the ray-tracing application, it is difficult to apply the same random phases to the same rays for each multielement antenna, as each antenna element may experience a different set of rays. Hence, generating random phases and realizations using random antenna displacements is a more appropriate (and better) approach in the ray model.

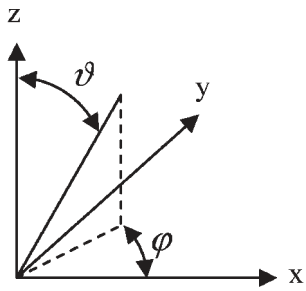

Fig. 8. Coordinate system used for the equations in generating random realizations of H.

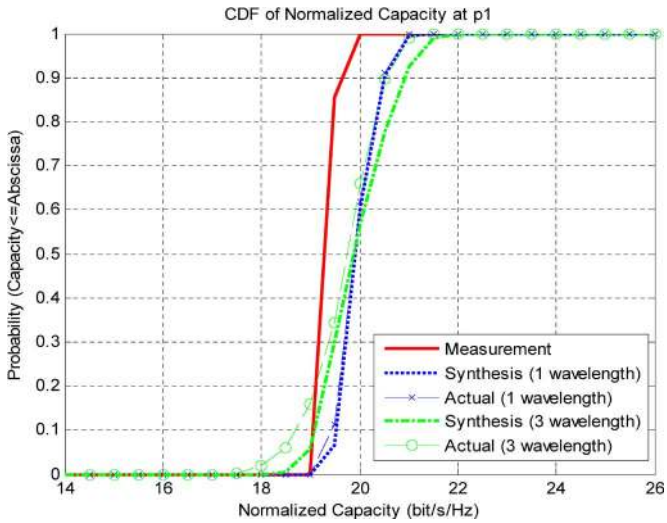

Fig. 9. CDF of normalized capacity for realizations with synthesis techniques and actual antenna displacement.

The synthesis technique in (2) is now compared with the accurate method of antenna displacement. A comparison of MIMO predictions is made at static location P1 in Fig. 5. There are 800 realizations studied. Fig. 9 shows a comparison of the cumulative distribution function (CDF) of the normalized capacity for the measured, synthesized, and actual displacement data. A fixed 20-dB signal-to-noise ratio (SNR) is assumed. A maximum displacement (using a sphere of diameter 1λ and 3λ) is used in the synthesis and actual techniques. It is shown that a maximum 1λ displacement produces a better agreement with the measurements. The normalized capacities for the case of a maximum 3λ displacement suffer from a larger variance, as the rays seen by the receiver experience larger magnitude

and phase changes. The actual and synthetic techniques have produced similar results in this case. As the maximum displacement distance is increased to 3λ, the difference between the results of the synthesis and the actual displacement techniques becomes larger. This is expected due to the greater difference in the directions of the rays when the displacement is large. Furthermore, differences in the LoS and NLoS scenarios for the rays between the synthesis and actual displacement case may contribute significantly to changes in the received field strength. Hence, the synthetic technique (with a maximum displacement diameter of 1λ) is used to generate multiple MIMO realizations for static receiver points in the MIMO validations given in Section IV.

IV. Ray-Tracing Comparison With MIMO Measurements

Initially, a range of standard comparisons are performed using predicted values of the average channel impulse response, the mean path loss, the mean root mean-square (rms) delay spread, and the mean Rician K-Factor. Comparisons are then extended to the MIMO channel, where the derived parameters such as the normalized theoretic MIMO capacity, the eigenstructure of the H-matrix, and the reciprocal condition number (RCN) are studied. Comparisons are made between the site-specific ray model prediction (using the tool described in Section II) and MIMO measurements at identical locations using the equipment and procedures described in Section III. An SNR of 20 dB was assumed together with equal power distribution to all transmit antennas.

The second part of the comparison process involves the prediction of PER using MIMO-OFDM extensions to the IEEE 802.11a physical layer [48]–[50]. SM and STBC versions of MIMO-OFDM are examined, with average PER calculations performed for a range of selected points and routes. The computation of the physical-layer PER using the measured and ray-traced MIMO channel data is unique to this paper. The aim of this paper is to demonstrate that the MIMO link-level performance can be accurately determined using channel data derived from a site-specific ray model.

Given N_T transmitters, N_R receivers, and K_f frequency samples, the channel matrix G is defined as the complex channel frequency response, where each element $g_{i,j,f}$ is the complex transmission coefficient between the jth transmitter element and the ith receiver element for the frequency sample f. H represents the normalized channel matrix [3]:

$$H = \frac{G}{\mathrm{NF}} \quad \text{where} \quad \mathrm{NF} = \sqrt{\frac{\sum_{i=1}^{N_R}\sum_{j=1}^{N_T}\sum_{f=0}^{K_f-1}|g_{i,j,f}|^2}{N_T N_R K_f}} \tag{6}$$

where NF represents the normalization factor, such that $E\{\|H\|^2\} = K_f N_T N_R$. The same normalization factor is used for all time realizations for the static points by averaging across the realization snapshots in a similar manner, providing that channels in the time snapshots are wide-sense-stationary (WSS). For moving studies, the normalization factors are calculated for each point separately. The normalized capacity C can de derived from this channel data, as shown as follows [1]–[4]:

$$\begin{aligned} C &= \frac{1}{K_f}\sum_{f=0}^{K_f-1}\log_2\left(\det\left(I_{N_R} + \frac{\rho}{N_T}H(f)H(f)^*\right)\right) \\ &= \frac{1}{K}\sum_{f=0}^{K_f-1}\sum_{n=1}^{N}\log_2\left(1+\frac{\rho}{N_T}\varepsilon_n(f)^2\right) \end{aligned} \tag{7}$$

where * represents the Hermitian transposition, I_{N_R} is the identity matrix, ρ is the average SNR, and $\varepsilon(f)$ is the square root of the eigenvalues of matrix $H(f)H(f)^*$ [or the singular values of matrix $H(f)$]. The RCN is as defined in [51] and [52].

Correlation in the $H(f)$-matrix plays a significant role in the calculation of channel capacity. This can be seen in the determinant of the channel correlation matrix $H(f)H(f)^*$ in (7). The link correlation matrix R_H is given in [3], as $R_H = E(\mathrm{vec}(H(f)) \times \mathrm{vec}(H(f)^*))$, where $\mathrm{vec}(\cdot)$ represents the matrix vector operation. Using the normalization in (6), on average, each individual link has unity power [53]. In order to obtain a good estimate of R_H from the measured or predicted channel matrices, many realizations are needed, provided the channel set is WSS (to ensure that the channel characteristics and, particularly, their correlations remain stationary) [3], [53]. A bandwidth of 20 MHz centered at 1.92 GHz is used in this comparison study. The considered bandwidth must be small enough for all of the 129 frequency snapshots to satisfy our WSS requirement. For each static point, averaging is performed over 800 time realizations and 129 frequency snapshots for each calculation of R_H. For moving points along a route, R_H is calculated for each point from an average of the 129 frequency snapshots. An absolute mean over all R_H is calculated for each route to obtain $\overline{|R_H|}$.

For a better visual illustration of the channel correlations, a transformed covariance matrix R_{tran} is defined by rearranging the elements of R_H in the manner described in the study in [3]. First, given two arbitrary matrices, A of dimensions $N_T \times N_T$ and B of dimensions $N_R \times N_R$, a permutation matrix T is defined which rearranges the elements of $A \otimes B$, where $\otimes$ is the Kronecker product, such that $T\mathrm{vec}(A \otimes B) = \mathrm{vec}(a \cdot b^{\mathrm{T}})$, where $a = \mathrm{vec}(A)$; $b = \mathrm{vec}(B)$. The permutation matrix T is then used to rearrange R_H to form R_{tran}, where $\mathrm{vec}(R_{\mathrm{tran}}) = T\mathrm{vec}(R_H)$. Both R_H and R_{tran} have dimensions $(N_T \times N_R, N_T \times N_R)$. Fig. 10 shows a plot of $|R_{\mathrm{tran}}|$ for a 4×8 ideal uncorrelated Rayleigh fading channel H_{ray}, where the transmission coefficients are independent and identically distributed (i.i.d.) complex Gaussian random variables, $H_{\mathrm{ray}} \in \mathrm{CN}(0,1)$.

It is shown in Fig. 10 that $|R_{\mathrm{tran}}|$ is divided into 4×8 block regions. Each block region is further subdivided into a set of 8×4 correlation coefficients. Each correlation coefficient is the complex correlation coefficient between transmission coefficients of index $([1,\ldots,N_R],[1,\ldots,N_T])$ within each block region and transmission coefficients of index $([1,\ldots,N_T],[1,\ldots,N_R])$ given by the block-region index. The rows of the block regions represent the transmitter index,

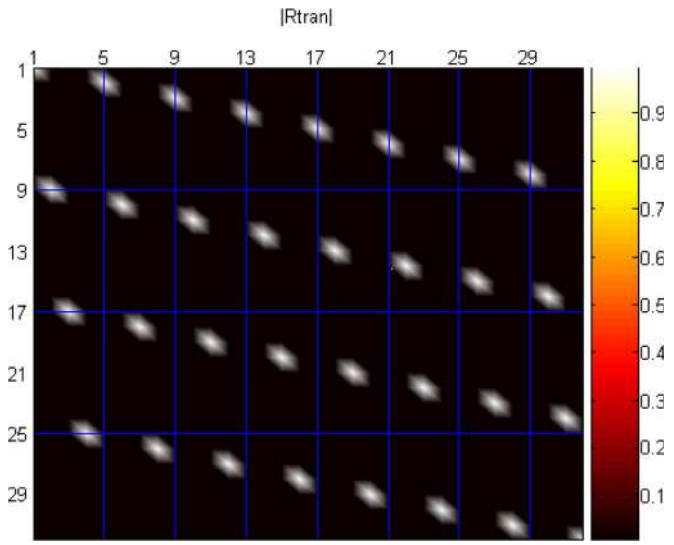

Fig. 10. Magnitude plot of $|R_{\mathrm{tran}}|$ for an ideal uncorrelated Rayleigh fading channel. Peaks show the autocorrelation points for each block region.

and the columns represent the receiver index. However, the rows of the coefficients within each block region represent the receiver index, and the columns represent the transmitter index. Hence, the autocorrelation points are shown as peaks in each block region. The trend of the decay in the correlation magnitude from the autocorrelation points provides a strong visualization of the correlations between the subchannels [3].

A. MIMO and Wideband Characteristics Comparison

Table II provides a summary of the mean path loss, Rician K-factor, and rms delay spread for each of the test locations considered in this paper. The table also includes a number of derived 4×8 MIMO parameters, such as the mean normalized capacity, a set of four eigenvalues, and the RCN parameter. In the case of the normalized capacity, a statistical CDF comparison is performed later in the section. Due to the limited measurement data set, this statistical analysis is not extended to the other parameters.

As shown in Table II, an absolute mean path-loss error of 2 dB is seen, which agrees well with the observed errors from a range of previous ray-tracing models [16]–[21], [23]–[26]. An absolute mean error in normalized theoretic MIMO capacity of 1.51 b/s/Hz was obtained (based on an average MIMO capacity of around 22 b/s/Hz). This result shows that the ray model is capable of providing accurate estimates of the theoretic MIMO capacity in this particular geographic region (i.e., values that agree well with those measured). The absolute mean error for the two most significant eigenvalues was seen to be less than 1 dB, which implies an accurate prediction of the MIMO eigenstructure. The absolute mean error for the RCN parameter was approximately 2.5 dB, with predictions accurately following the trends seen in our measured data.

Overall, the values quoted in Table II demonstrate that our MIMO ray-tracing predictions enjoy a good agreement with the measured results in the region. Most importantly, the prediction errors for the eigenvalues are small, and hence, the correlation structures in the MIMO subchannels are well predicted [4]. This strong level of agreement also supports our polarization-modeling approach, since the transmitter used in our measurement program was dual polar.

On average, the ray-tracing model was seen to under predict the MIMO capacity by around 10%. This was mainly due to a lack of decorrelated fading in the predicted channels, as evident in the larger mean error of the two least significant eigenvalues and the lower RCN values. This error is likely to arise from a lack of scatter in the model (partly due to the use of a simplified database). The theoretic MIMO capacity is a random variable in this case, with its practical limit given by assuming an i.i.d. complex Gaussian channel matrix. Perfectly decorrelated fading channels generate a set of equal magnitude eigenvalues (for a normalized channel matrix). Fig. 11 shows a comparison of the measured and predicted CDF of the normalized capacity at point P2 (4×8 MIMO channel) against that of an ideal uncorrelated Rayleigh (i.i.d. Rayleigh) fading channel. As expected, the predicted capacity is lower than the measured value, and both are less than the ideal i.i.d. Rayleigh case.

As described previously, the channel covariance matrix R_{tran} shows the spatial correlation characteristic of each subchannel, and this can provide a visual understanding of the subchannel correlations. Fig. 12 shows a comparison of $\overline{|R_{\mathrm{tran}}|}$ as generated from the Medav measurements and the ray-tracing predictions for channel M1. As shown in Table II, the average difference in the normalized capacity between the measurement and prediction along route M1 is just 0.1 b/s/Hz (based on a measured value of 23.95 b/s/Hz). The eigenvalues are also shown to closely agree, demonstrating that the ray model is able to recreate the detailed MIMO channel structure along this route. Fig. 12 shows that the measured and predicted $\overline{|R_{\mathrm{tran}}|}$ agree well, with a difference in the absolute average correlation coefficients of just 0.093. The predicted channels can be seen to suffer from higher correlation values at the receiving elements, since the vertical correlation coefficients in each block region are higher than those for the measured channels [3]. In both channels, the correlation between the first and second transmitter elements, or the third and fourth transmitter elements, are high; this is shown by the horizontally decaying magnitude of the correlation coefficients from the autocorrelation peak in each block region (a higher magnitude spread is seen in the left or right horizontal region at the autocorrelation peak in each block region). This shows that, even though those two sets of transmitter elements are dual polarized, they still experience high correlation levels since they are in the same location and suffer correlated spatial fading in a similar scattering environment. On the other hand, low correlation is experienced between element set (1, 2) and element set (3, 4), due to the uncorrelated spatial fading at an antenna separation distance of 20λ.

Fig. 13 shows a comparison of $\overline{|R_{\mathrm{tran}}|}$ for route M6, where the predicted and measured normalized capacities have produced a larger average error of -2.39 b/s/Hz; with an RCN difference of -3.73 dB. Here, the predicted channels suffer higher levels of correlation across both the transmit and receive elements, with the high-magnitude correlation coefficients decaying away in both the horizontal and vertical direction from the autocorrelation peak. An absolute average correlation

TABLE II
SUMMARY OF MEAN VALUE OF MIMO AND WIDEBAND CHARACTERISTICS ON ALL LOCATIONS

Location	Path Loss (dB)	K Factor	RMS Delay Spread (ns)	N. Capacity (bits/s/Hz)	ε_1^2 (dB)	ε_2^2 (dB)	ε_3^2 (dB)	ε_4^2 (dB)	RCN (dB)
P1 (Mea)	101.51	3.33	254.99	19.44	14.69	3.13	-3.41	-14.55	-29.22
P1 (Pre)	103.80	1.24	291.81	19.97	14.60	4.38	-5.444	-11.25	-25.72
P2 (Mea)	101.51	3.3	259.36	19.48	14.67	3.39	-3.34	-14.48	-29.16
P2 (Pre)	102.46	2.75	242.2	16.85	14.75	2.71	-12.06	-18.51	-33.09
P3 (Mea)	108.37	1.95	281.04	23.67	13.94	6.67	3.97	-9.79	-23.50
P3 (Pre)	108.86	0.65	235.22	20.97	14.18	7.20	-4.00	-12.03	-25.63
P4 (Mea)	116.14	1.14	272.24	24.54	13.90	7.40	1.88	-4.74	-18.18
P4 (Pre)	118.74	0.76	306.81	22.72	13.58	9.18	-2.18	-8.51	-21.59
P5 (Mea)	93.67	18.45	168.71	16.54	14.94	-2.15	-8.30	-15.42	-30.39
P5 (Pre)	97.56	4.63	169.76	15.18	14.94	-1.46	-12.65	-20.49	-35.36
M1 (Mea)	114.30	0.47	320.39	23.95	13.89	7.65	1.39	-6.21	-19.39
M1 (Pre)	116.59	0.57	242.49	23.85	13.74	8.45	0.17	-6.15	-19.25
M2 (Mea)	117.98	0.49	317.97	24.59	13.74	7.94	2.37	-4.96	-18.20
M2 (Pre)	117.04	0.69	301.22	24.43	13.59	8.79	0.56	-5.02	-18.12
M3 (Mea)	103.56	2.4	253.08	22.19	14.17	7.18	-2.80	-8.39	-22.38
M3 (Pre)	106.60	2.23	278.91	22.25	14.15	7.10	-2.83	-8.13	-22.08
M4 (Mea)	106.53	1.62	271.65	23.40	14.03	6.92	1.52	-7.97	-21.41
M4 (Pre)	108.47	1.24	247.27	21.40	14.02	7.81	-4.41	-10.19	-23.66
M5 (Mea)	112.11	0.81	252.67	23.56	14.10	6.45	1.81	-7.34	-20.98
M5 (Pre)	112.88	0.58	265.12	21.94	14.17	7.00	-2.74	-8.67	-21.77
M6 (Mea)	105.12	0.76	373.02	24.87	13.63	8.44	1.60	-4.20	-17.25
M6 (Pre)	109.55	3.16	290.82	22.48	14.23	6.12	-1.02	-7.70	-20.98
M7 (Mea)	121.62	1.32	360.28	24.90	13.67	8.15	1.59	-3.97	-16.88
M7 (Pre)	121.25	2.76	279.38	22.14	14.04	7.51	-1.91	-8.61	-22.02
Mean Absolute Error (Mean Error)	**2.00 (1.78)**	**1.92 (1.23)**	**42.02 (27.86)**	**1.51 (1.41)**	**0.18 (-0.05)**	**0.92 (-0.30)**	**3.90 (3.90)**	**2.54 (1.94)**	**2.53 (1.86)**

* (Mea) denotes measurement, (Pre) denotes prediction.

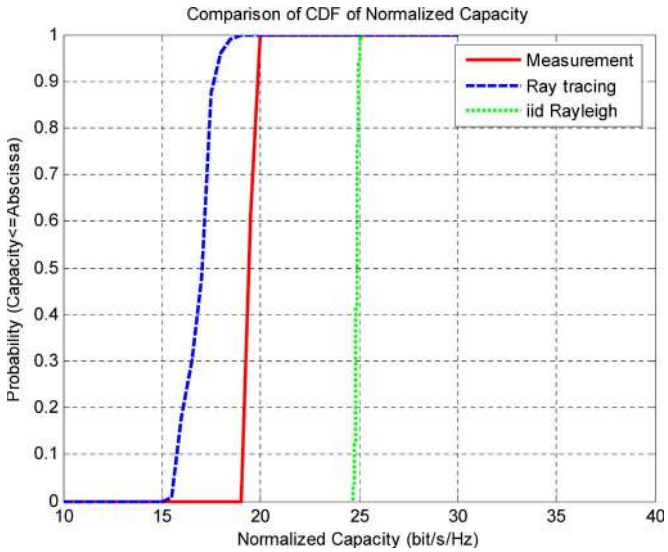

Fig. 11. CDF of normalized MIMO capacity (4 × 8) at P2 (measured, predicted, and theoretic i.i.d. Rayleigh).

coefficient difference of 0.18 is seen in this case. Overall, the predicted channels produce higher correlation levels between the subchannels, with an absolute average correlation coefficient error of 0.15 and an average correlation coefficient error of −0.045. It is these higher correlation values that result in the lower capacity predictions (see Fig. 14). The lower predicted decorrelation values are thought to result from a number of factors. These include the environment database, the electromagnetic models, and the antenna model. It should be noted that these factors are also the main contributor for the prediction error in conventional ray-tracing models [39], [54], [55].

The complexity of the environment database determines the level of detail used to represent the real world. Database complexity is also directly proportional to the computational cost of ray tracing. The richness of the scatter in a modeled environment will always be poorer than the real world. Fades in a rich scattering environment tend to be more spatially decorrelated (due to higher angular spreads), and hence, real-world channels result in higher MIMO channel capacities [4]. Geometrical errors in the database objects and the positioning of the transmitter and/or receiver can also have a significant impact on the accuracy of the received power prediction. Finally, errors in the electromagnetic models (such as UTD, Fresnel reflection coefficients, and scattering model) used for each propagation mechanism have a direct impact on the received power, and hence, the prediction of the channel matrix.

Antenna modeling includes the modeling of the antenna pattern as well as any mutual coupling effects that result from near-field propagation. The antenna patterns that are used in this validation study were obtained via anechoic chamber measurements for the receiving monopoles [see Fig. 7(b)] and via synthetic-pattern generation for the transmitting antennas [see Fig. 7(a)]. In general, the use of measured antenna patterns (instead of synthetic patterns) produced higher levels of fading decorrelation [56]. This is mainly due to the pattern diversity that results from the complexity of the measured side-lobes. Measured patterns result in lower spatial-radiation-pattern correlation compared to simplified synthetic patterns. Fig. 15 shows a comparison of normalized capacity for the

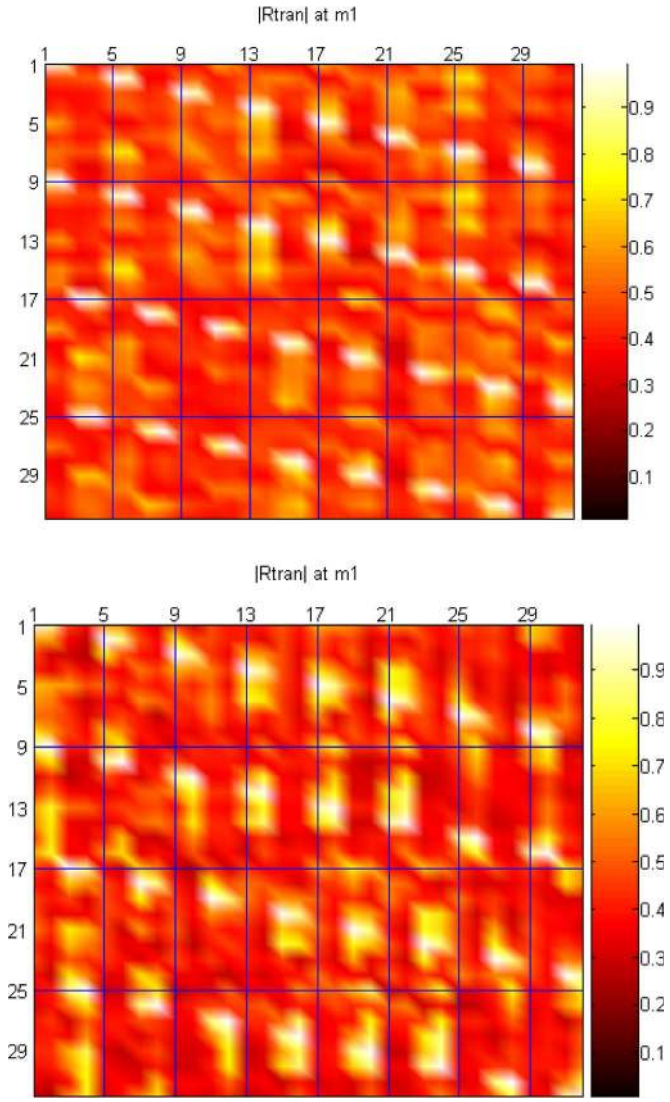

Fig. 12. Magnitude plot of $|R_{\mathrm{tran}}|$ for (left) measured and (right) predicted channels at M1.

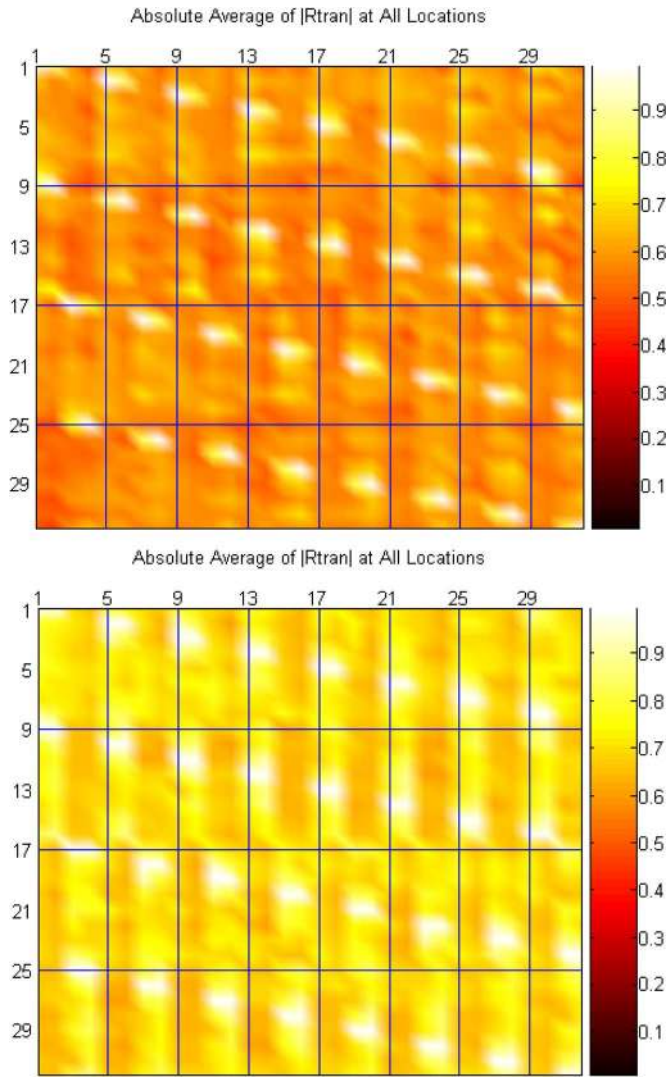

Fig. 13. Magnitude plot of $|R_{\mathrm{tran}}|$ for (left) measured and (right) predicted channels at M6.

cases where measured and synthetic antenna patterns were used at location P5 in Fig. 5. The antenna pattern, which is shown in Fig. 7(b), and a synthesized monopole that exhibits an ideal half-dipole pattern, with an infinite ground plane, are now used to represent the receiver monopoles. The transmit antenna patterns remained unchanged in this paper (i.e., based on synthetic patterns). It can be seen that, in this particular case, the measured antenna pattern improves the normalized capacity (the mean error improves by around 0.6 b/s/Hz). Fig. 16 provides a comparison of R_{tran} for the cases of measured and synthesized receiver-antenna patterns. It can be seen that the measured antenna patterns produce lower correlation coefficients around the autocorrelation peaks, compared to the case with ideal synthesized patterns. An average difference in the correlation coefficient of -0.036 is seen with this data. Thus, the use of synthesized transmit-antenna patterns in our comparison study may well account for a large part of the prediction error. Furthermore, it should be noted that our studies ignore mutual coupling effects, which, in some cases, are reported to have a significant impact on MIMO capacity [57]. While the work reported in [56] and [57] also considers the use of ray tracing to study the performance of MIMO systems, this prior work focuses on the modeling of the antenna elements. In this paper, we focus on comparing the predicted MIMO channel response (and a number of derived parameters) to those from practical measurements in an urban environment. Such comparisons have not been previously reported in the literature.

B. MIMO-OFDM Physical-Layer Performance Comparison

In this section, we compare the average PER as a function of E_b/N_0 using the measured and predicted MIMO channels. The physical layer assumes MIMO-OFDM with parameters closely based on the IEEE 802.11a. Both STBC and SM schemes are considered [5]–[14]. The aim is to demonstrate that ray-traced MIMO channels are a viable substitute for measured channel data when determining physical-layer performance. The 16-QAM with 1/2 rate coding and ideal channel knowledge is assumed. A total of 4896 channel snapshots are used from seven measurement routes (each with 128 snapshots) and five

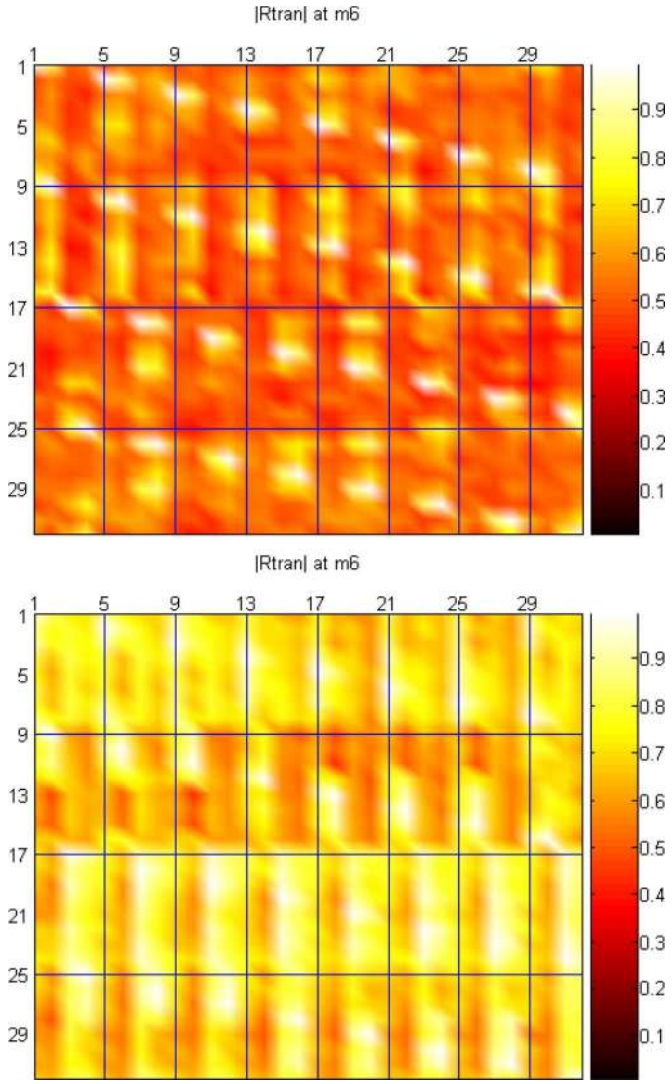

Fig. 14. Magnitude plot of overall absolute averaged $|R_{tran}|$ for all (left) measured and (right) predicted channels.

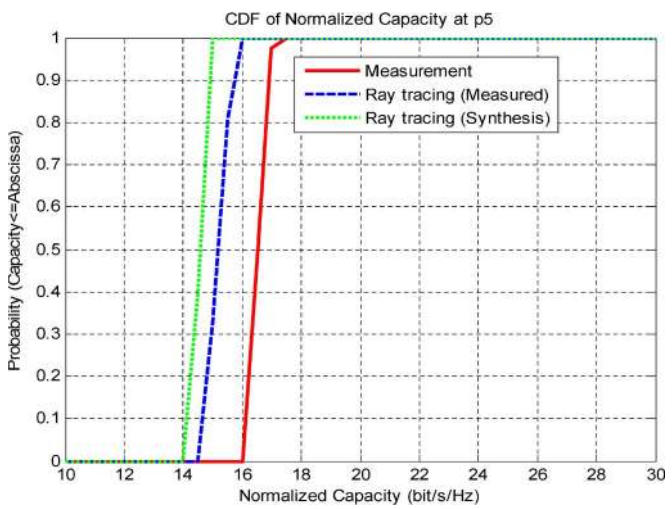

Fig. 15. Comparison of CDF of normalized capacity at P5 with measured and synthetic antenna pattern.

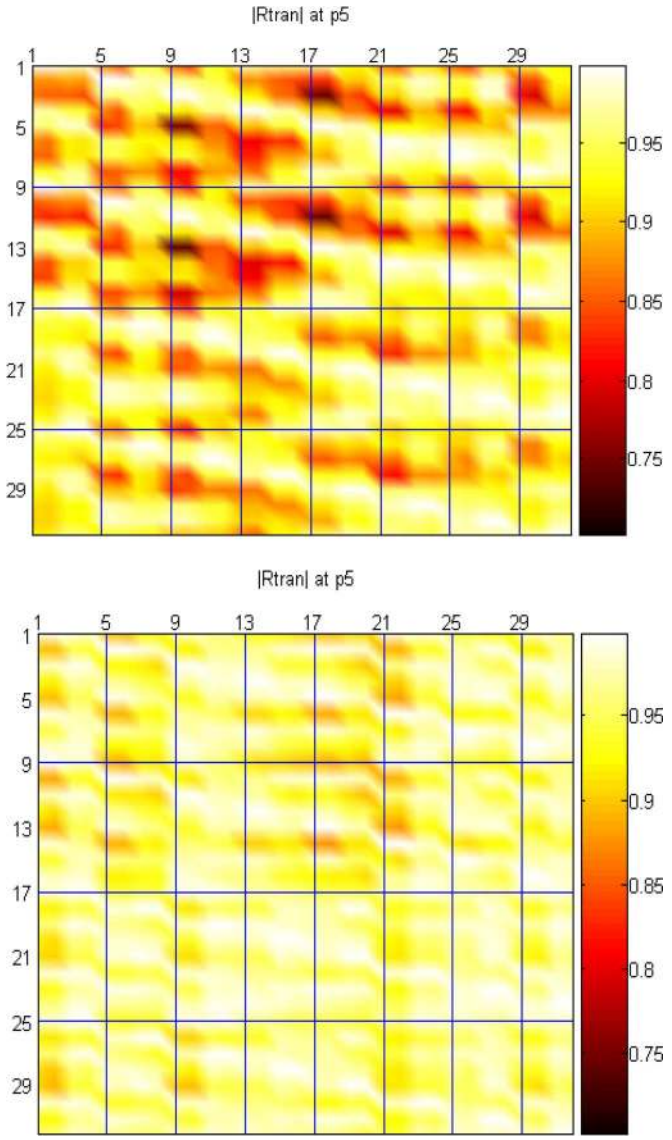

Fig. 16. Magnitude plot of $|R_{\mathrm{tran}}|$ at P5 for the case of using measured and synthetic antenna pattern.

static measurement points (each with 800 snapshots). In the extraction of the power-delay profile, a dynamic threshold window of 30 dB is used (measured from the power peak). This threshold is used to remove weak paths and any noise floor present in the measured channels. A 4×4 MIMO channel configuration is used, with antennas selected from the four cross elements of the eight-element Uniform Circular Array (UCA) receiver. A detailed description of the physical-layer parameters and the detection algorithms can be found in [48]–[50].

Simulations were performed for all locations; however, due to space restrictions, only subsets of the results are presented in this paper. Fig. 17 shows the comparison of PER for locations P2, P5, and M3 using the SM and STBC schemes. The PER performance was seen to vary significantly from location to location when the SM scheme was applied. This occurred for both measured and predicted channels and implies that the SM schemes are very sensitive to the MIMO channel structure. This occurs partly because SM systems do not explicitly exploit diversity gain [7]–[14]. In comparison, the STBC scheme gave

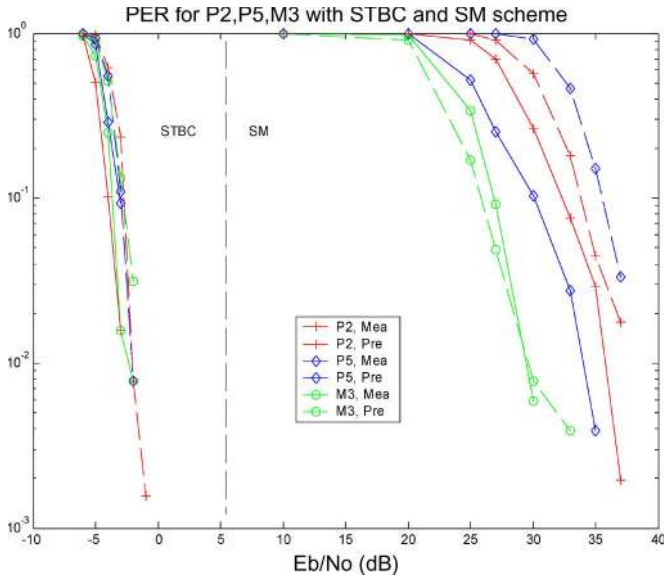

Fig. 17. PER for locations P2, P5, and M3 (SM and STBC). (solid lines) Measured. (dashed lines) Predicted.

TABLE III
CORRELATION COEFFICIENT BETWEEN E_b/N_0 AND VARIOUS CHARACTERISTICS

Channels	RMS DS	K-Factor	N.Capacity	RCN
Measured	-0.73	0.75	-0.76	-0.91
Predicted	-0.75	0.63	-0.89	-0.93

very stable results. The average PER using the predicted and measured channel data was seen to be in close agreement. A mean E_b/N_0 error (compared to PER results from the measured channel data) of 4 and 1 dB was calculated for the SM and STBC schemes, respectively. As shown in Table II, the RCNs as calculated from the measurements, and ray-tracing predictions for locations P2 and M3 are in close agreement, and this is reflected in the PER results for SM. The small difference in the RCNs for location P5 results in a larger variation in the PER performances for the predicted and measurement MIMO channels.

Table III shows the correlation between the E_b/N_0 (at a PER of 1%) and the rms delay spread, K-factor, normalized capacity, and RCN. It can be seen that the high rms delay spread, high normalized capacity, low RCN, and low K-factor generally correlate to a better PER performance for SM systems [9]. Since near-identical correlations are shown in Table III using the measured and predicted channel data, for our dataset, we conclude that the complex relationship between PER and MIMO channel structure is faithfully replicated in our ray-traced data. Clearly, more detailed-measurement campaigns are required to confirm this result in the wider sense.

V. CONCLUSION

An efficient ray-tracing propagation model has been developed and its predictions compared against a set of measured data in a dense urban environment. The model used a detailed geographic database comprising 3-D building data, foliage, and terrain heights. Detailed corner and rooftop diffraction was modeled, together with specular reflection and scattering from buildings and terrain. These features were particularly important in the MIMO case, where the modeling of rich scatter was found to be important. The model combined a range of sophisticated optimization techniques to accelerate the ray-path-finding process. These features enabled the model to perform fast propagation analysis in complex environments. These acceleration methods are particularly welcome for MIMO systems, where exhaustive ray tracing is performed for all antenna-element pairs.

Comparison with MIMO measurement data showed good agreement in the prediction of wideband and MIMO characteristics. An average path-loss error of 2 dB and a normalized capacity error of 1.5 b/s/Hz (less than 10% of the measured capacity) were seen. Comparisons also extended to the eigen and correlation structure of the MIMO channel in both LoS and NLoS locations. The measurement data included the use of dual polar antenna elements, and the model was shown to successfully predict all major trends.

The antenna pattern was shown to have a strong impact on performance. While reasonable agreement was achieved using synthetic patterns, in our analysis, the best predictions were achieved using measured antenna patterns from an anechoic chamber. Measured patterns were found to have more detailed side- and back-lobe information, which in this particular case, helped to improve the quality of our predictions.

Unique to this paper, our comparisons were extended to analyze the PER performance of two popular MIMO-OFDM systems (SM and STBC). Channel data was measured at 1.92 GHz and also generated using the ray model for identical locations and antenna structures. Comparison of PER results showed good agreement, with errors in E_b/N_0 at a PER of 1% varying from 1 to 4 dB between the measured and modeled channels. The SM schemes were seen to be far more sensitive to small variations in correlation, K-factor, and/or rms delay spread.

Our studies indicate that ray models of this type can be used to generate statistically relevant MIMO channel data for any antenna structure and deployment strategy. Given the close agreement seen here with measured MIMO channel data, we conclude that ray models could be used to optimize the configuration of future MIMO systems (i.e., the number of antennas, the antenna geometry, the use of polarization, the form of modulation and coding, etc.). Alternatively, models of this type could be used to aid the site-specific deployment of emerging networks, such as those based on 802.11n or 802.16e. Further validation studies (ideally in other environments and with a broader set of measurements) are required to confirm these findings.

ACKNOWLEDGMENT

The authors would like to thank Prof. M. Beach and S. E. Foo for performing the channel measurements used in this paper.

REFERENCES

[1] G. J. Foschini and M. J. Gans, "On limits of wireless communications in a fading environment when using multiple antennas," *Wireless Pers. Commun.*, vol. 6, no. 3, pp. 311–335, Mar. 1998.
[2] I. E. Telatar, "Capacity of multi-antenna Gaussian channels," *Eur. Trans. Telecommun.*, vol. 10, no. 6, pp. 585–595, Nov. 1999.

[3] D. P. McNamara, "Characterisation and investigation of multiple-input multiple output wireless communication channels," P.h.D. dissertation, Univ. Bristol, Bristol, U.K., Mar. 2003.

[4] D. Shiu, G. Foschini, M. Gans, and J. Khan, "Fading correlation and its effect on the capacity of multielement antenna systems," *IEEE Trans. Commun.*, vol. 48, no. 3, pp. 502–513, Mar. 2000.

[5] G. J. Foschini, "Layered space-time architecture for wireless communication in a fading environment when using multi-element antennas," *Bell Labs Tech. J.*, vol. 1, no. 2, pp. 41–59, Autumn 1996.

[6] G. J. Foschini, D. Chizhik, M. J. Gans, C. Papadias, and R. A. Valenzuela, "Analysis and performance of some basic space-time architectures," *IEEE J. Sel. Areas Commun.*, vol. 21, no. 3, pp. 303–320, Apr. 2003.

[7] S. M. Alamouti, "A simple transmit diversity technique for wireless communications," *IEEE J. Sel. Areas Commun.*, vol. 16, no. 8, pp. 1451–1458, Oct. 1998.

[8] V. Tarokh, N. Seshadri, and A. R. Calderbank, "Space-time codes for high data rate wireless communications: Performance criterion and code construction," *IEEE Trans. Inf. Theory*, vol. 44, no. 2, pp. 744–765, Mar. 1998.

[9] C. Williams, Ed., "Antenna array technology and MIMO systems," *Report for Ofcom Spectral Efficiency Scheme*, 2004. [Online]. Available: http://www.ofcom.org.uk

[10] H. Bolcskei, D. Gesbert, and A. J. Paulraj, "On the capacity of OFDM-based spatial multiplexing systems," *IEEE Trans. Commun.*, vol. 50, no. 2, pp. 225–234, Feb. 2002.

[11] N. Boubaker, K. B. Lataief, and R. D. Murch, "Performance of BLAST over frequency-selective wireless communication channels," *IEEE Trans. Commun.*, vol. 50, no. 2, pp. 196–199, Feb. 2002.

[12] A. Lozano and C. Papadias, "Space-time receiver for wideband BLAST in rich-scattering wireless channels," in *Proc. IEEE VTC—Spring*, 2000, pp. 186–190.

[13] X. Zhuang, F. W. Vook, S. Rouquette-Leveil, and K. Gosse, "Transmit diversity and spatial multiplexing in four transmit antenna OFDM," in *Proc. IEEE ICC*, May 2003, pp. 2316–2320.

[14] H. M. Karkhanechi and B. C. Levy, "Spatial multiplexing and diversity gain in OFDM-based MIMO systems," in *Proc. IEEE Wireless Commun. Technol.*, Oct. 2003, pp. 299–301.

[15] D. A. McNamara, C. W. I. Pistorius, and J. A. G. Malherbe, *Introduction to the Uniform Geometrical Theory of Diffraction*. Norwood, MA: Artech House, 1990.

[16] G. E. Athanasiadou, A. R. Nix, and J. P. McGeehan, "A microcellular ray-tracing propagation model and evaluation of its narrow-band and wide-band predictions," *IEEE J. Sel. Areas Commun.*, vol. 18, no. 3, pp. 322–335, Mar. 2000.

[17] T. Rautiainen, G. Wolfle, and R. Hoppe, "Verifying path loss and delay spread predictions of a 3D ray tracing propagation model in urban environments," in *Proc. 56th IEEE Veh. Technol. Conf.*, Sep. 2002, pp. 2470–2474.

[18] K. Rizk, R. Valenzuela, S. Fortune, D. Chizhik, and F. Gardiol, "Lateral, full 3D and vertical plane propagation in microcells and small cells," in *Proc. 48th IEEE Veh. Technol. Conf.*, May 1998, pp. 998–1003.

[19] G. Wolfle, R. Hoppe, and F. M. Landstorfer, "Radio network planning with ray optical propagation models for urban, indoor, and hybrid scenarios," in *Proc. 11th IEEE Wireless Conf.*, Calgary, AB, Canada, Jul. 1999, pp. 515–522.

[20] M. C. Lawton and J. P. McGeehan, "The application of a deterministic ray launching algorithm for the prediction of radio channel characteristics in small cell environments," *IEEE Trans. Veh. Technol.*, vol. 43, no. 4, pp. 955–969, Nov. 1994.

[21] G. Liang and H. L. Bertoni, "A new approach to 3-D ray tracing for propagation prediction in cities," *IEEE Trans. Antennas Propag.*, vol. 46, no. 6, pp. 853–863, Jun. 1998.

[22] *Local and metropolitan area networks, Part 11: Wireless LAN Medium Access Control (MAC) and Physical Layer (PHY) specifications, Amendment 1: High-speed physical layer in the 5 GHz band*. IEEE Std. 802.11a-1999

[23] K. H. Ng, E. Tameh, and A. R. Nix, "An advanced multi-element microcellular ray tracing model," in *Proc. 1st Int. Symp. Wireless Commun. Syst.*, Sep. 2004, pp. 438–442.

[24] K. H. Ng, E. Tameh, and A. R. Nix, "Modelling and performance prediction for multiple antenna systems using enhanced ray tracing," in *Proc. IEEE Wireless Commun. and Netw. Conf.*, Mar. 2005, pp. 933–937.

[25] K. H. Ng, E. Tameh, and A. R. Nix, "A new hybrid geometrical optics and radiance based scattering model for deterministic ray tracing model," in *Proc. IEEE ICC*, May 2005, pp. 2168–2172.

[26] K. H. Ng, E. Tameh, and A. R. Nix, "A new heuristic geometrical approach for finding non-coplanar multiple edge diffraction ray paths," *IEEE Trans. Antennas Propag.* , vol. 54, no. 9, pp. 2669–2672, Sep. 2006.

[27] R. J. Luebbers, "A heuristic UTD slope diffraction coefficient for rough lossy wedges," *IEEE Trans. Antennas Propag.*, vol. 37, no. 2, pp. 206–211, Feb. 1989.

[28] P. D. Holm, "A new heuristic UTD diffraction coefficient for nonperfectly conducting wedges," *IEEE Trans. Antennas Propag.*, vol. 48, no. 8, pp. 1211–1219, Aug. 2000.

[29] COST 235, *Radiowave propagation effects on next generation fixed services terrestrial telecommunications systems*, 1996, Brussels, Belgium: Commission Eur. Union. Final Rep.

[30] R. Hoppe, P. Wertz, G. Wolfle, and F. M. Landstorfer, "Fast and enhanced ray optical propagation modeling for radio network planning in urban and indoor scenarios," in *Proc. MPRG Wireless Pers. Commun. Symp.*, VA, Jun. 2000.

[31] F. A. Agelet, F. P. Fontan, and A. Formella, "Fast ray tracing for microcellular and indoor environments," *IEEE Trans. Magn.*, vol. 33, no. 2, pp. 1484–1487, Mar. 1997.

[32] R. P. Torres, L. Valle, M. Domingo, and S. Loredo, "An efficient ray-tracing method for radiopropagation based on the modified BSP algorithm," in *Proc. IEEE Veh. Technol. Conf.*, Amsterdam, The Netherlands, Sep. 1999, pp. 1967–1971.

[33] M. Deloura, *Game Programming Gems*. Hingham, MA: Charles River Media, 2000.

[34] A. Hoult and G. Simmons. (2004, May 6). *Engine Programming With BSP Tree*. [Online]. Available: http://www.gameinstitute.com

[35] M. F. Catedra, J. Perez, F. S. Adana, and O. Gutierrez, "Efficient ray-tracing techniques for three-dimensional analyses of propagation in mobile communications: Application to picocell and microcell scenarios," *IEEE Antennas Propag. Mag.*, vol. 40, no. 2, pp. 15–28, Apr. 1998.

[36] M. F. Iskander and Z. Yun, "Propagation prediction models for wireless communication systems," *IEEE Trans. Microw. Theory Tech.*, vol. 50, no. 3, pp. 662–673, Mar. 2002.

[37] "Characterisation of the outdoor MIMO channels in the 2 GHz ULTRA band," Deliverable IST-2001-32549-D421, EU IST Project *ROMANTIK*.

[38] C. A. Balanis, *Antenna Theory: Analysis and Design*. Hoboken, NJ: Wiley, 1982.

[39] G. E. Athanasiadou and A. R. Nix, "Investigation into the sensitivity of the power predictions of a microcellular ray tracing propagation model," *IEEE Trans. Veh. Technol.*, vol. 49, no. 4, pp. 1140–1151, Jul. 2000.

[40] D. D. Kerr, "Propagation of short radio waves," in *IEE Electromagnetic Wave Series*, vol. 24. Los Altos, CA: Peninsula, 1987.

[41] I. Cuinas and M. G. Sanchez, "Permittivity and conductivity measurements of building materials at 5.8 GHz and 41.5 GHz," *Wireless Pers. Commun.*, vol. 20, no. 1, pp. 93–100, Jan. 2002.

[42] P. Beckmann and A. Spizzichino, *The Scattering of Electromagnetic Waves from Rough Surfaces*. New York: Pergamon, 1963.

[43] P. A. Bello, "Characterization of randomly time-variant linear channels," *IEEE Trans. Commun.*, vol. COM-11, no. 4, pp. 360–393, Dec. 1963.

[44] R. Kattenbach, "Statistical modeling of small-scale fading in directional radio channels," *IEEE J. Sel. Areas Commun.*, vol. 20, no. 3, pp. 584–592, Apr. 2002.

[45] R. S. Thoma, D. Hampicke, A. Richter, G. Sommerkorn, A. G. Schneider, U. Trautwein, and W. U. Wirnitzer, "Identification of time-variant directional mobile radio channels," *IEEE Trans. Instrum. Meas.*, vol. 49, no. 2, pp. 357–364, Apr. 2000.

[46] J. G. Proakis, *Digital Communications*, 4th ed. New York: McGraw-Hill, 2001.

[47] A. F. Molisch, M. Steinbauer, M. Toeltsch, E. Bonek, and R. S. Thoma, "Capacity of MIMO systems based on measured wireless channels," *IEEE J. Sel. Areas Commun.*, vol. 20, no. 3, pp. 561–569, Apr. 2002.

[48] A. Doufexi, E. Tameh, A. Molina, and A. R. Nix, "Application of sectorised antennas and STBC to increase the capacity of hot spot WLANs in an interworked WLAN/3G network," in *Proc. IEEE VTC—Spring*, Milan, Italy, May 2004, pp. 2962–2966.

[49] A. Doufexi, E. Tameh, C. Williams, M. Beach, A. Prado, and A. R. Nix, "Spectrum efficiency benefits of MIMO systems in hot spot scenarios," in *Proc. WWRF12 Meeting*, Toronto, ON, Canada, Nov. 2004.

[50] A. Doufexi, A. Prado, S. Armour, A. R. Nix, and M. Beach, "Use of space time block codes and spatial multiplexing using TDLS channel estimation to enhance the throughput of OFDM based WLANs," in *Proc. IEEE Veh. Technol. Conf.—Spring*, Jeju, Korea, Apr. 2003, pp. 704–708.

[51] V. Erceg, P. Soma, D. Baum, and A. J. Paulraj, "Capacity obtained from multiple-input multiple-output channel measurements in fixed wireless environments at 2.5 GHz," in *Proc. Int. Conf. Commun.*, May 2002, vol. 1, pp. 396–400.

[52] M. D. Batariere, T. K. Blankenship, J. F. Kepler, T. P. Krauss, I. Lisica, S. Mukthavaram, J. W. Porter, T. A. Thomas, and F. W. Vook, "Wideband MIMO mobile impulse response measurements at 3.7 GHz," in *Proc. IEEE 55th Veh. Technol. Conf.—Spring*, 2002, pp. 26–30.
[53] K. Sakaguchi, H. Chua, and K. Araki, "MIMO channel capacity in an indoor line-of-sight (LOS) environment," *IEICE Trans. Commun.*, vol. E88-B, no. 7, pp. 3010–3019, Jul. 2005.
[54] K. Rizk, J. F. Wagen, and F. Gardiol, "Influence of database accuracy on two-dimensional ray-tracing-based predictions in urban microcells," *IEEE Trans. Veh. Technol.*, vol. 49, no. 2, pp. 631–642, Mar. 2000.
[55] S. S. Wang and J. D. Reed, "Analysis of parameter sensitivity in a ray tracing propagation environment," in *Proc. IEEE VTC*, Chicago, IL, May 4–7, 1997, pp. 805–809.
[56] K. R. Dandekar, H. Ling, and G. Xu, "Experimental study of mutual coupling compensation in smart antenna applications," *IEEE Trans. Wireless Commun.*, vol. 1, no. 3, pp. 480–487, Jul. 2002.
[57] K. R. Dandekar and R. W. Heath, "Modeling realistic electromagnetic effects on MIMO system capacity," *Electron. Lett.*, vol. 38, no. 25, pp. 1624–1625, Dec. 2002.

Kah Heng Ng received the B.Eng. and Ph.D. degrees from the University of Bristol, Bristol, U.K., in 2002 and 2006, respectively. His Ph.D. study focused on urban radio-wave-propagation modeling for multiple-antenna systems.

He is currently a Systems Engineer at Picochip Designs Ltd., Bath, U.K. His research interests include the development and application of ray tracing and the analysis of multiple-input–multiple-output communication systems.

Eustace K. Tameh received the B.Sc. degree (with honors) in electronic engineering and mathematics from Keele University, Staffordshire, U.K., in 1994. He joined the University of Bristol, Bristol, U.K., in 1994 and received the Ph.D. degree in wide area propagation prediction and planning in 1998.

In 1997, he became a Research Associate with the University of Bristol, working on research projects on propagation modelling and cellular network design. In 2006, he joined ProVision Communication Technologies Ltd, Bristol, where he leads the development of a range of RF planning tools. His current research interests are in the development of novel planning techniques for broadband systems and multisystem integration for third-generation-and-beyond networks.

Angela Doufexi received the B.Sc. degree in physics from the University of Athens, Panepistimiopolis, Illisia, Greece, in 1996, the M.Sc. degree in electronic engineering from Cardiff University, Wales, U.K., in 1998, and the Ph.D. degree from the Centre for Communications Research, University of Bristol, Bristol, U.K., in 2002.

She is currently a Lecturer in wireless networks at the University of Bristol. She has worked on a number of projects including the European IST-SATURN, ROMANTIK, WCAM, and ASTRALS projects. Her research interests include orthogonal frequency-division multiplexing (OFDM) and OFD multiple-access systems, multiuser diversity and resource allocation, wireless LANs and WiMax (physical layer and medium-access control), space-time coding and multiple-input–multiple-output, fourth-generation communications systems, and multimedia transmission. She has published over 50 journal and conference papers in these areas.

Mythri Hunukumbure received the B.Sc. degree in electronic and telecommunications engineering from the University of Moratuwa, Moratuwa, Sri Lanka in 1998, and the M.Sc. and Ph.D. degrees from the University of Bristol, Bristol, U.K.

He was with the Wireless Research Group, University of Bristol. His research has encompassed the appraisal of code orthogonality and space-time signal-processing technology in third-generation mobile systems. In addition, he has been actively involved in the European COST 273, IST-SATURN, and Mobile Virtual Centre of Excellence research programs.

Andrew R. Nix received the B.Eng. and Ph.D. degrees from the University of Bristol, Bristol, U.K., in 1989 and 1993, respectively.

He was with the Centre for Communications Research, University of Bristol, as a member of the lecturing staff, and currently, as a Professor of wireless-communication systems. His main research interests include broadband wireless communications, radio-wave-propagation modeling, cellular-network optimization, and advanced digital modulation/reception techniques. He has managed numerous European Union, Engineering and Physical Sciences Research Council, and Department of Trade and Industry funded projects and published in excess of 250 Journal and Conference papers.